

Understanding current-driven dynamics of magnetic Néel walls in heavy metal/ferromagnetic metal/oxide trilayers

Mei Li^{1,2}, Jianbo Wang^{2,4} and Jie Lu^{3,4}

¹ Physics Department, Shijiazhuang University, Shijiazhuang, Hebei 050035, China

² School of Physics and Technology, Center for Electron Microscopy and MOE Key Laboratory of Artificial Micro- and Nano-structures, Wuhan University, Wuhan 430072, China

³ College of Physics and Information Engineering, Hebei Advanced Thin Films Laboratory, Hebei Normal University, Shijiazhuang 050024, China

⁴ Authors to whom any correspondence should be addressed.

E-mail: wang@whu.edu.cn, jlu@hebtu.edu.cn

Abstract. We consider analytically current-driven dynamics of magnetic Néel walls in heavy metal/ferromagnetic metal/oxide trilayers where strong spin-orbit coupling and interfacial Dzyaloshinskii-Moriya interaction (i-DMI) coexist. We show that field-like spin-orbit torque (FL-SOT) with effective field along $\mathbf{n} \times \hat{\mathbf{J}}$ (\mathbf{n} being the interface normal and $\hat{\mathbf{J}}$ being the charge current direction) and i-DMI induced torque can both lead to Walker breakdown suppression meanwhile leaving the wall mobility (velocity versus current density) unchanged. However, i-DMI itself can not induce the “universal absence of Walker breakdown” (UAWB) while FL-SOT exceeding a certain threshold can. Finitely-enlarged Walker limits before UAWB are theoretically calculated and well explain existing data. In addition, change in wall mobility and even its sign-inversion can be understood only if the anti-damping-like (ADL) SOT is appended. For Néel walls in ferromagnetic-metal layer with both perpendicular and in-plane anisotropies, we have calculated the respective modifications of wall mobility under the coexistence of spin-transfer torque, SOTs and i-DMI. Analytics shows that in trilayers with perpendicular anisotropy strong enough spin Hall angle and appropriate sign of i-DMI parameter can lead to sign-inversion in wall mobility even under small enough current density, while in those with in-plane anisotropy this only occurs for current density in a specific range.

Keywords: spin-orbit coupling, interfacial Dzyaloshinskii-Moriya interaction, spin-orbit torque, magnetic Néel walls, current-driven dynamics

Submitted to: *New J. Phys.*

1. Introduction

Pure current-induced domain wall propagation in magnetic nanostructures has attracted intensive attention for decades starting from academic interests in understanding the interplay between itinerant spinful electrons and localized magnetic moments[1, 2, 3, 4]. In monolayer ferromagnetic nanostrips, in-plane currents drive domain walls to propagate along the direction of electron flow through the spin transfer process[5, 6, 7, 8, 9, 10, 11, 12, 13, 14, 15], which leads to promising applications in future magnetic racetrack memories[16, 17], shift registers[18, 19] and memristors[20, 21], etc. However, in these monolayers the wall velocity is at most 10^2 m/s even when the current density is up to 10^8 A/cm². This comes from the fact that spin transfer torques (STTs) therein can not be strong as the exchange energy avoids abrupt changes in magnetization texture. To improve the current efficiency, the current-perpendicular-to-plane (CPP) configuration in narrow and long spin valves is proposed [22, 23, 24]: to reach the same velocity level (10^2 m/s), the current density for “planar polarizer” case is reduced to 10^7 A/cm² while that for “perpendicular polarizer” can even be lowered to 10^6 A/cm². However, the rapidly increasing CPP cross-section area largely offsets the decrease in current density. Even if the current is forced to focus on wall region, precise dynamical synchronization in real experiments remains challenging.

Over the past decade, in heavy metal/ferromagnetic metal/oxide (HM/FMM/Oxide) trilayers, axial domain wall propagation in FMM layer with perpendicular magnetic anisotropy (PMA) or in-plane magnetic anisotropy (IPMA) driven by axial currents are experimentally observed[25, 26, 27, 28, 29, 30, 31, 32, 33, 34, 35, 36, 37, 38, 39, 40, 41]. In certain case (Pt/Co/AlO_x), walls can move at a high velocity up to 400 m/s when current density is around 10^8 A/cm²[37]. More interestingly, walls with certain polarity can even move in the direction of charge current[33, 34, 35, 36, 37, 38, 39, 40, 41], which is also confirmed by numerical simulations [42, 43, 44, 45]. To understand these findings, spin-orbit torques (SOTs) from strong spin-orbit coupling (SOC) in these trilayers are proposed [46, 47, 48, 49, 50, 51, 52, 53, 54, 55, 56, 57, 58, 59]. Suppose $\hat{\mathbf{J}}$ is the charge current direction and \mathbf{n} is interface normal. Mathematically, SOTs can be decomposed into two perpendicular components: (a) $\propto \mathbf{m} \times (\hat{\mathbf{J}} \times \mathbf{n})$ which is odd in magnetization direction \mathbf{m} and usually referred to as field-like (FL) torque; (b) $\propto \mathbf{m} \times [\mathbf{m} \times (\hat{\mathbf{J}} \times \mathbf{n})]$ which is even in \mathbf{m} and usually called anti-damping-like (ADL) torque. Physically, two typical mechanisms are of most importance: the “spin Hall torques” from the spin Hall effect (SHE)[60] in HM layer and the “Rashba torques” from the structure inversion asymmetry (SIA) at the HM/FMM interface. In early literatures, ADL-SOTs are believed to stem mostly from bulk SHE while FL-SOTs are mainly attributed to interfacial Rashba SOC. However, recent works based on scattering-related mechanisms[52, 53, 54, 55, 56] and intrinsic Berry curvature[57, 58] reveal that Rashba SOC can cause FL and ADL SOTs with similar strength. Meantime, quantum tunneling of spin current from HMs to FMMs[59] allows SHE to provide FL and ADL SOTs with comparable magnitude. So far, physical source of SOTs is still a hot issue under debate[61, 62, 63, 64]. Besides

Rashba SOT, SIA in these trilayers also leads to the interfacial Dzyaloshinskii-Moriya interaction (i-DMI)[65, 66, 67], which favors a canting of the spins and stabilizes Néel walls in FMM layers.

Meantime, analytics with Lagrangian functional[68, 69, 70] and simulations[71, 72, 73, 74, 75, 76, 77] based on Landau-Lifshitz-Gilbert (LLG) dynamical equation[78] have been performed to explain Néel wall dynamics in HM/FMM/Oxide trilayers in the framework of one-dimensional collective coordinate model (1D-CCM). All these works focus on two novel features in experiments: (i) Walker breakdown suppression thus high wall velocity and (ii) wall motion opposed to electron flow and the corresponding “polarity sensitivity”. Historically, the Rashba-SOC-induced FL-SOT is first proposed to explain both novelties[71, 72, 73]. In addition, the novelty (ii) is also reproduced numerically by only ADL-SOTs from SHE in IPMA systems[74]. In 2017, Risinggård and Linder proposed the “universal absence of Walker breakdown” (UAWB) of Néel walls in PMA systems for strong enough Rashba or SHE effect[79] with the coexistence of i-DMI. However, to our knowledge there are no explicit analytical expressions for finitely enlarged Walker limit before the occurrence of UAWB. In addition, theoretical criteria for sign-inversion in wall mobility (velocity versus current density) and the corresponding “polarity selection rule” for trilayers with both PMA and IPMA are absent. The role of i-DMI in all these processes is also unclear. Explorations to these issues constitute the main content of this paper.

The rest of this paper is organized as follows. In section 2 the system set up and its modelization are briefly introduced. Also, the static Néel wall configurations and the dynamical equations for FMM layers with both PMA and IPMA are presented. Then in section 3 within 1D-CCM we provide analytical expressions of finitely enlarged Walker limits by FL-SOT and/or i-DMI induced torque before UAWB. In section 4, theoretical criteria for sign-inversion in wall mobility and the corresponding “polarity selection rule” for FMM layers with both PMA and IPMA are provided under the coexistence of ADL-SOT and i-DMI. Finally, concluding remarks are provided in the last section.

2. Modeling and preparations

We consider an HM/FMM/Oxide trilayer with a domain wall formed in FMM layer. Generally, the FMM layer has strong PMA or IPMA. Typical example for the former (latter) case is Co (NiFe). Meanwhile, the HM layer is composed of Pt or Ta in most experiments. For both cases, the in-plane charge current flows along the long axis of the strip with density j_a . As passing through the trilayer, the charge current splits into two parts. Suppose j_F (j_H) to be the current density in FMM (HM) layer. A simple circuit model tells us that $j_F = j_a(t_F+t_H)\sigma_F/(t_F\sigma_F+t_H\sigma_H)$ and $j_H = j_a(t_F+t_H)\sigma_H/(t_F\sigma_F+t_H\sigma_H)$, where t_F (t_H) and σ_F (σ_H) are the thickness and conductivity of the FMM (HM) layer, respectively. For the most common FMM (Co, Ni, Fe) and HM (Pt, Ta, Ir) materials, the conductivity varies from 10 to 20 ($\mu\Omega\text{m}$)⁻¹. For simplicity in this work, we set $\sigma_F = \sigma_H$ thus $j_F = j_H = j_a$.

For trilayers with PMA, the coordinate system is depicted in figure 1a: \mathbf{e}_x is along the long axis of strip in which charge current flows, \mathbf{e}_z is the interface normal and $\mathbf{e}_y = \mathbf{e}_z \times \mathbf{e}_x$. The easy (hard) axis of the FMM layer with PMA lies in \mathbf{e}_z (\mathbf{e}_y) direction. While for trilayers with IPMA (see figure 1b), \mathbf{e}_z (\mathbf{e}_y) is along the long axis (interface normal) of the strip which is the easy (hard) axis, and $\mathbf{e}_x = \mathbf{e}_y \times \mathbf{e}_z$.

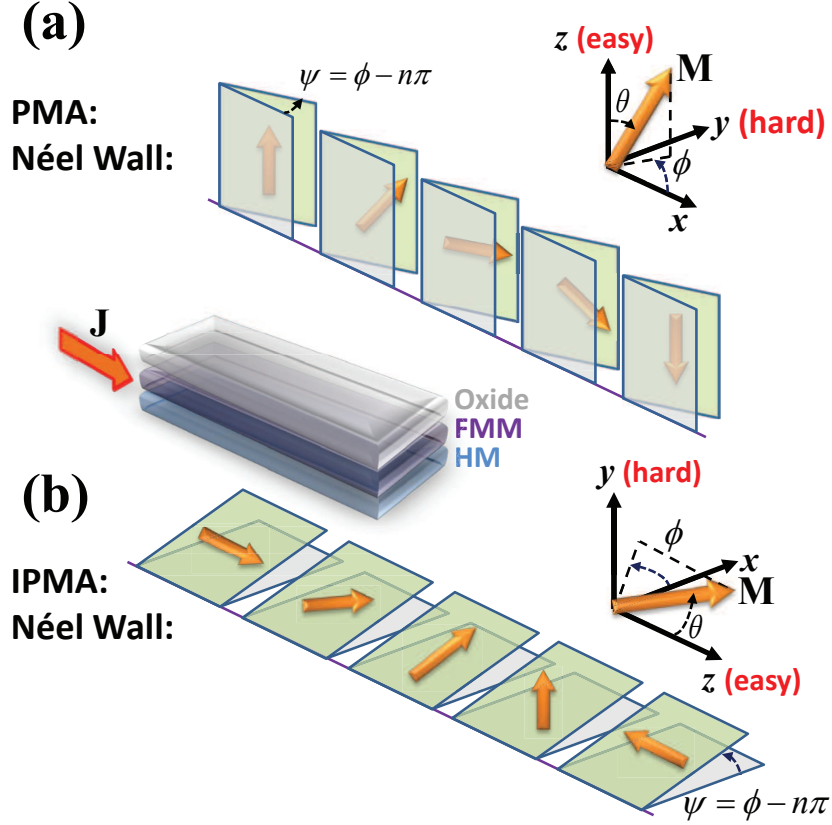


Figure 1. (Color online) Sketch of a typical HM/FMM/Oxide trilayer in which a Néel wall is formed in FMM layer with (a) PMA and (b) IPMA, as a result of energy minimization. The corresponding coordinate system is depicted at the up-right corner in each subfigure. In each case, gray planes describe the planar ϕ -distribution of static magnetization texture. When in-plane charge current \mathbf{J} is applied, magnetization vectors will be driven to tilt from their static locations by ψ , as indicated by the green planes. This sketch is inspired by figure 1 in Ref. [68].

2.1. Dynamical equation

In thin enough strips, most of the nonlocal magnetostatic energy can be described by local quadratic terms of $M_{x,y,z}$ via three average demagnetization factors. Thus in the absence of any external magnetic field, the total magnetic energy density functional takes the following form

$$\mathcal{E}_{\text{tot}}[\mathbf{M}] = \mathcal{E}_{\text{ex}} + \mathcal{E}_{\text{DM}} + \mathcal{E}_{\text{ani}}, \quad (1)$$

in which $\mathcal{E}_{\text{ex}} = J(\nabla\mathbf{m})^2$ and $J(> 0)$ is the exchange stiffness. The i-DMI contribution is $\mathcal{E}_{\text{DM}} = D[(\mathbf{m} \cdot \mathbf{n})(\nabla \cdot \mathbf{m}) - (\mathbf{m} \cdot \nabla)(\mathbf{m} \cdot \mathbf{n})]$, where D is the magnitude of i-DMI vector and \mathbf{n} is the interface normal. The total magnetic anisotropy energy density is $\mathcal{E}_{\text{ani}} = (\mu_0 M_s^2/2)[-k_E(\mathbf{m} \cdot \mathbf{n}_E)^2 + k_H(\mathbf{m} \cdot \mathbf{n}_H)^2]$, in which $\mathbf{n}_E(\mathbf{n}_H)$ and $k_E(k_H)$ are the unit vector and total anisotropy coefficient in easy (hard) axis, respectively. The time evolution of magnetization texture $\mathbf{M}(\mathbf{r}, t) \equiv M_s \mathbf{m}(\mathbf{r}, t)$ with fixed saturation magnetization M_s is governed by the generalized LLG equation

$$\frac{\partial \mathbf{m}}{\partial t} = -\gamma \mathbf{m} \times \mathbf{H}_{\text{eff}} + \alpha \left(\mathbf{m} \times \frac{\partial \mathbf{m}}{\partial t} \right) + \mathbf{T}_{\text{STT}} + \mathbf{T}_{\text{SOT}}, \quad (2)$$

where $\mathbf{H}_{\text{eff}} = -(\delta\mathcal{E}_{\text{tot}}/\delta\mathbf{m})/(\mu_0 M_s)$ is the effective field, γ and α are the gyromagnetic ratio and phenomenological damping coefficient, respectively.

Note \mathbf{T}_{STT} only appears for inhomogeneous magnetization texture with [6, 7]

$$\mathbf{T}_{\text{STT}} = B_J \frac{\partial \mathbf{m}}{\partial \hat{\mathbf{J}}} - \beta B_J \mathbf{m} \times \frac{\partial \mathbf{m}}{\partial \hat{\mathbf{J}}}, \quad (3)$$

where $B_J = g_e \mu_B P j_F / (2e M_s) \approx \mu_B P j_a / (e M_s)$, with e, g_e, μ_B being the absolute value of electron charge, the electron g -factor and Bohr magneton, respectively. P is the spin polarization of j_F . The two terms in the right hand side of equation (3) are the so-called adiabatic and non-adiabatic STTs, respectively. They are the continuous counterparts of the Slonczeswki [2] and FL STTs in spin valves. β is the dimensionless coefficient describing the relative strength of the nonadiabatic STT and usually of the same order as α . Previous works have verified that in traveling-wave mode STT-driven walls always move in the direction of electron flow, which is attributed to the existence of nonadiabatic ingredient (β -term).

Generally SOTs have both FL and ADL components. Each component includes the contributions from both SHE and Rashba SOC. In this work we focus on domain wall dynamics rather than physical sources of SOTs, thus \mathbf{T}_{SOT} can be written as

$$\mathbf{T}_{\text{SOT}} = -\gamma H_{\text{FL}} \mathbf{m} \times (\mathbf{n} \times \hat{\mathbf{J}}) - \gamma H_{\text{ADL}} \mathbf{m} \times \left[\mathbf{m} \times (\mathbf{n} \times \hat{\mathbf{J}}) \right]. \quad (4)$$

Both H_{FL} and H_{ADL} stem from various physical processes and have the unit of magnetic field. Their ratio varies in a wide range for different trilayer systems.

2.2. Static wall configuration

In the absence of external charge current, the magnetization texture eventually evolves into some equilibrium state. The ground state is the one with a single domain which is of little interest. Alternatively, the metastable state with a wall separating two magnetic domains is of great importance for both academic and industrial interests. In this subsection, we provide static wall configurations for trilayers with both PMA and IPMA.

First we focus on FMM layers with PMA (see figure 1a), thus $\mathbf{n} = \mathbf{n}_E = \mathbf{e}_z$ and $\mathbf{n}_H = \mathbf{e}_y$. For statics, the magnetization is no longer function of time but only varies

with location along x -axis in 1D-CCM. By dropping a constant $-k_E\mu_0M_s^2/2$, the total energy density turns to

$$\begin{aligned} \mathcal{E}_{\text{PMA}}[\mathbf{M}] = & \frac{1}{2}\mu_0M_s^2 \sin^2 \theta (k_E + k_H \sin^2 \phi) + J \left[(\theta')^2 + \sin^2 \theta (\phi')^2 \right] \\ & + D (\cos \phi \theta' - \sin \theta \cos \theta \sin \phi \phi'), \end{aligned} \quad (5)$$

where θ (ϕ) is the polar (azimuthal) angle of the magnetization vector (see figure 1a) and a “prime” means d/dx . Physically, a static wall configuration should provide a minimum of the total magnetic energy. For this purpose, first we should have $\phi' \equiv 0$ to suppress the exchange energy, which makes ϕ a collective coordinate. Then we introduce the Lagrangian functional $L = \int \mathcal{L} d^3\mathbf{r}$ with Lagrangian density

$$\mathcal{L} = \frac{\mu_0M_s}{\gamma} \frac{\partial \phi}{\partial t} (1 - \cos \theta) - \mathcal{E}_{\text{tot}}[\mathbf{M}], \quad (6)$$

and the boundary condition

$$\mathbf{m}(x = \mp\infty) = \pm\eta\mathbf{e}_z, \quad (7)$$

with $\eta = \pm 1$ coming from the two-fold symmetry of magnetic anisotropy in easy axis and can be viewed as the topological charge of this wall. The corresponding Euler equation

$$\frac{d}{dx} \left(\frac{\partial \mathcal{L}}{\partial (d\theta/dx)} \right) - \frac{d}{d\theta} \mathcal{L} = 0 \quad (8)$$

together with the static condition $\partial\phi/\partial t = 0$ lead to

$$\frac{d^2\theta}{dx^2} = \frac{\sin \theta \cos \theta}{\Delta^2(\phi)}, \quad \Delta(\phi) = \sqrt{\frac{2J}{\mu_0M_s^2 (k_E + k_H \sin^2 \phi)}}. \quad (9)$$

Its soliton solution is the well-known Walker profile[80]

$$\ln \tan \frac{\theta}{2} = \eta \frac{x - x_0}{\Delta(\phi)}, \quad (10)$$

where x_0 denotes the wall center position. Putting it back into (5), one has

$$\mathcal{E}_{\text{PMA}}[\mathbf{M}] = \mu_0M_s^2 \sin^2 \theta (k_E + k_H \sin^2 \phi) + \eta D \cos \phi \frac{\sin \theta}{\Delta(\phi)}. \quad (11)$$

The energy minimization strategy then naturally demands that $\sin \phi = 0$ and $\cos \phi = -\eta \text{sgn}(D)$, where “sgn” is the sign function. This means that in PMA systems, the i-DMI favors Néel wall and further selects wall polarity (sign of $\langle m_y \rangle$).

Next we turn to IPMA systems (see figure 1b) in which $\mathbf{n} = \mathbf{n}_H = \mathbf{e}_y$ and $\mathbf{n}_E = \mathbf{e}_z$. After similar process, we obtain the same θ -profile as in equation (10) except for $x(x_0) \rightarrow z(z_0)$, under which the total energy density of IPMA systems becomes

$$\mathcal{E}_{\text{IPMA}}[\mathbf{M}] = \mu_0M_s^2 \sin^2 \theta (k_E + k_H \sin^2 \phi) - \eta D \sin \phi \frac{\sin \theta}{\Delta(\phi)}. \quad (12)$$

To minimize the first term in the right hand side of the above equation, one also need $\sin \phi(z) \equiv 0$ which eliminates the i-DMI term. This implies that in IPMA systems, the Néel wall is naturally the result of energy minimization strategy and the i-DMI does not select wall polarity.

2.3. General scalar LLG equations

By taking into account the conversion between Descartes and spherical coordinate systems, the vectorial LLG equation (2) is transformed into the following scalar pair

$$\begin{aligned} \left(\dot{\theta} + \alpha \sin \theta \dot{\phi}\right) - B_J (\theta' + \beta \sin \theta \phi') &= \gamma \tilde{A}, \\ \left(\sin \theta \dot{\phi} - \alpha \dot{\theta}\right) - B_J (\sin \theta \phi' - \beta \theta') &= \gamma \tilde{B}. \end{aligned} \quad (13)$$

For PMA systems, one has

$$\begin{aligned} \tilde{A} &= A + H_{\text{FL}} \cos \phi + H_{\text{ADL}} \cos \theta \sin \phi, \\ \tilde{B} &= B + H_{\text{ADL}} \cos \phi - H_{\text{FL}} \cos \theta \sin \phi, \end{aligned} \quad (14)$$

with

$$\begin{aligned} A &= \frac{2D}{\mu_0 M_s} \sin \theta \sin \phi \theta' + \frac{2J}{\mu_0 M_s \sin \theta} (\phi' \sin^2 \theta)' - k_{\text{H}} M_s \sin \theta \sin \phi \cos \phi, \\ B &= M_s \sin \theta \cos \theta (k_{\text{E}} + k_{\text{H}} \sin^2 \phi) + \frac{2D}{\mu_0 M_s} \sin^2 \theta \sin \phi \phi' \\ &\quad - \frac{2J}{\mu_0 M_s} [\theta'' - (\phi')^2 \sin \theta \cos \theta], \end{aligned} \quad (15)$$

where a “dot (prime)” means $\partial/\partial t$ ($\partial/\partial x$).

While for IMPA system, alternatively one has

$$\begin{aligned} \tilde{A} &= A - H_{\text{FL}} \sin \phi + H_{\text{ADL}} \cos \theta \cos \phi, \\ \tilde{B} &= B - H_{\text{ADL}} \sin \phi - H_{\text{FL}} \cos \theta \cos \phi, \end{aligned} \quad (16)$$

with

$$\begin{aligned} A &= \frac{2D}{\mu_0 M_s} \sin \theta \cos \phi \theta' + \frac{2J}{\mu_0 M_s \sin \theta} (\phi' \sin^2 \theta)' - k_{\text{H}} M_s \sin \theta \sin \phi \cos \phi, \\ B &= M_s \sin \theta \cos \theta (k_{\text{E}} + k_{\text{H}} \sin^2 \phi) + \frac{2D}{\mu_0 M_s} \sin^2 \theta \cos \phi \phi' \\ &\quad - \frac{2J}{\mu_0 M_s} [\theta'' - (\phi')^2 \sin \theta \cos \theta], \end{aligned} \quad (17)$$

in which a “prime” means $\partial/\partial z$.

3. Walker breakdown suppression by FL-SOT and/or i-DMI

In this section we present analytical expressions of finitely enlarged Walker limit before UAWB in the absence of ADL-SOT. We will show the different roles of FL-SOT and i-DMI in modulating the STT-initiated traveling-wave mode of domain wall.

3.1. Brief review of wall dynamics under pure STT

For a Néel wall in an isolated FMM and driven by pure STTs from axial currents ($H_{\text{FL}} = H_{\text{ADL}} \equiv 0$, $D \equiv 0$ and $B_J \neq 0$), the static wall profile can be generalized to [6, 7]

$$\ln \tan \frac{\theta}{2} = \frac{\eta}{\Delta(\phi)} \left[r - \int_0^t v(\tau) d\tau \right], \quad \phi = \phi(t), \quad (18)$$

where $r = x(z)$ for PMA (IPMA) case, $\Delta(\phi)$ is the same as in equation (9) and $v(t)$ is the wall velocity. Then for trilayers with both PMA and IPMA, we have

$$\tilde{A} = -k_{\text{H}}M_s \sin \theta \sin \phi \cos \phi, \quad \tilde{B} = 0. \quad (19)$$

Putting back into the scalar LLG equations, one has

$$\begin{aligned} \frac{v(t)}{\Delta(\phi)} &= \frac{\eta\gamma}{2(1+\alpha^2)} H_{\text{K}} \sin 2\phi - \frac{1+\alpha\beta}{1+\alpha^2} \frac{B_J}{\Delta(\phi)}, \\ \dot{\phi} &= -\frac{\alpha\gamma}{2(1+\alpha^2)} H_{\text{K}} \sin 2\phi + \frac{\alpha-\beta}{1+\alpha^2} \frac{\eta B_J}{\Delta(\phi)}, \end{aligned} \quad (20)$$

with $H_{\text{K}} \equiv k_{\text{H}}M_s$. By eliminating the “ $H_{\text{K}} \sin 2\phi$ ” term, $v(t)$ and $\dot{\phi}$ are directly related as

$$v(t) = -\frac{\eta\Delta(\phi)}{\alpha} \dot{\phi} - \frac{\beta}{\alpha} B_J. \quad (21)$$

By setting $\dot{\phi} = 0$ in the above equation, the Walker limit

$$J_{\text{W}} \equiv \frac{eM_s}{\mu_B P} \cdot \frac{\Delta\gamma H_{\text{W}}}{|\alpha-\beta|}, \quad H_{\text{W}} \equiv \frac{\alpha H_{\text{K}}}{2} \quad (22)$$

is obtained as the result of constraint $|\sin 2\phi| \leq 1$. Here we neglect the breathing effect of dynamical wall width $\Delta(\phi)$. Equations (20) and (21) show that when $|J_e| \leq J_{\text{W}}$ the wall propagates along electron-flow direction in a traveling-wave mode with the velocity $-\beta B_J/\alpha$ and the tilting angle

$$\phi = \phi_0 + \frac{1}{2} \arcsin \left[\eta \text{sgn}(\alpha - \beta) \frac{j_a}{J_{\text{W}}} \right], \quad (23)$$

where $\phi_0 = \arccos[-\eta \text{sgn}(D)]$ for PMA case and $\phi_0 = k\pi, k \in \mathbb{Z}$ for IPMA case. Obviously when $\alpha = \beta$, $J_{\text{W}} = +\infty$ implying the occurrence of UAWB.

3.2. General framework under the coexistence of STT, FL-SOT and *i*-DMI

First we focus on trilayers with PMA. As illustrated, a traveling wave described by equation (18) can always be adopted to perform analytics[79]. Under this wall profile, \tilde{A} and \tilde{B} in equation (14) becomes

$$\begin{aligned} \tilde{A} &= \frac{2\eta D}{\mu_0 M_s \Delta} \sin^2 \theta \sin \phi - \frac{H_{\text{K}}}{2} \sin \theta \sin 2\phi + H_{\text{FL}} \cos \phi, \\ \tilde{B} &= -H_{\text{FL}} \cos \theta \sin \phi. \end{aligned} \quad (24)$$

Putting back to the scalar LLG equations, and then integrating over the whole strip ($\int_{-\infty}^{+\infty} \sin \theta dx/\Delta \equiv \int_0^\pi d\theta$), one has

$$\begin{aligned} \frac{v(t)}{\Delta(\phi)} &= \frac{\eta\gamma \mathcal{H}(H_{\text{K}}, H_{\text{FL}}, D, \phi)}{2(1+\alpha^2)} - \frac{1+\alpha\beta}{1+\alpha^2} \frac{B_J}{\Delta(\phi)}, \\ \dot{\phi} &= -\frac{\alpha\gamma \mathcal{H}(H_{\text{K}}, H_{\text{FL}}, D, \phi)}{2(1+\alpha^2)} + \frac{\alpha-\beta}{1+\alpha^2} \frac{\eta B_J}{\Delta(\phi)}, \end{aligned} \quad (25)$$

with the functional

$$\mathcal{H}(H_{\text{K}}, H_{\text{FL}}, D, \phi) \equiv H_{\text{K}} \sin 2\phi - \frac{\eta\pi D}{\mu_0 M_s \Delta} \sin \phi - \pi H_{\text{FL}} \cos \phi. \quad (26)$$

Obviously, equation (25) shares the same structure with equation (20), except for the substitution of “ $H_K \sin 2\phi$ ” by the functional $\mathcal{H}(H_K, H_{\text{FL}}, D, \phi)$, thus leads to the rediscovery of equation (21). *This means neither the FL-SOT nor the i-DMI can change the wall mobility. However they do suppress the Walker breakdown thus increase the upper limit of wall velocity in traveling-wave mode.*

To see this, we first define

$$a \equiv \pi \frac{H_{\text{FL}}}{H_K}, \quad b \equiv \frac{\eta\pi D}{\mu_0 M_s H_K \Delta}. \quad (27)$$

Then by setting $\dot{\phi} = 0$, the second line in equation (25) provides

$$\sin 2\phi - a \cos \phi - b \sin \phi = \eta \text{sgn}(\alpha - \beta) \frac{j_a}{J_W}. \quad (28)$$

Next we set $(H_{\text{FL}})_W$ as the absolute effective field strength when $|j_a| = J_W$. Then by defining

$$a_W \equiv \frac{\pi (H_{\text{FL}})_W}{H_K} > 0, \quad (29)$$

equation (28) is rewritten as

$$\frac{j_a}{J_W} = \frac{\sin 2\phi - b \sin \phi}{\eta \text{sgn}(\alpha - \beta) + a_W \cos \phi}. \quad (30)$$

By maximizing the absolute value of its right hand side, we get the modified Walker limit $J_W^{\text{FL+DM}}$.

If $a_W > 1$, $j_a/J_W \rightarrow \infty$ when $\cos \phi = -\eta \text{sgn}(\alpha - \beta)/a_W$ thus leading to infinite $J_W^{\text{FL+DM}}$ (i.e. UAWB), which is essentially the same as that from equation (8) of Ref. [79]. When $a_W = 1$ and $b \neq 2$, without losing generality we set “ $\eta \text{sgn}(\alpha - \beta) \equiv -1$ ”. As $\phi \rightarrow 0^+$ one has $|j_a/J_W| \approx |2\phi^{-1}(2 - \phi^2 - b)| \rightarrow +\infty$. Note that a special parameter combination “ $a_W = 1$ and $b = 2$ ” leads to $|j_a/J_W| = 2|\sin \phi|$, which gives a doubled Walker limit. Except for this special case, one would see that finite $J_W^{\text{FL+DM}}$ can only exist for $0 < a_W < 1$.

On the other hand for trilayers with IPMA, the only difference is that equation (28) turns to

$$\sin 2\phi + a \sin \phi - b \cos \phi = \eta \text{sgn}(\alpha - \beta) \frac{j_a}{J_W}, \quad (31)$$

meanwhile leaving all other definitions and discussions unchanged. However, for both PMA and IPMA cases, it is hopelessly complicated in mathematics if finite a and b coexist. In the following subsections, we provide explicit analytics on finite enlargement of Walker limit in the presence of either finite a (FL-SOT) or finite b (i-DMI).

3.3. Coexistence of STT and FL-SOT

First we set $b = 0$ which means the i-DMI is absent. For PMA systems, we set $\cos \phi \equiv u \in [-1, +1]$ and define a new function $\mathcal{F}(u)$ from (30) as

$$\mathcal{F}(u) \equiv (j_a/J_W)^2 = 4u^2(1 - u^2)/(1 - a_W u)^2. \quad (32)$$

Obviously, $\mathcal{F}(u)$ is nonnegative. It equals to zero when and only when $u = 0$ or ± 1 . To find its extrema, by setting $\mathcal{F}'(u) = 0$ one obtains four extremal sites:

$$u_{k=1,2,3} = \frac{1}{3a_W} \left[2 + 4 \cos \frac{\theta + (2k-3)\pi}{3} \right], \quad \theta = \arccos \left(\frac{27}{16} a_W^2 - 1 \right), \quad (33)$$

and $u_4 = 0$. Obviously u_4 is the minimum point which can be verified by $\mathcal{F}''(u_4) > 0$. When $a_W \rightarrow 0^+$, direct calculation yields that $u_1 \approx 2/a_W - a_W/4 \rightarrow +\infty$ and $u_{2,3} \approx \pm 1/\sqrt{2} + a_W/8 \rightarrow \pm 1/\sqrt{2}$, implying that $u_{2,3}$ are the two maximum points satisfying $-1 < u_3 < 0 < u_2 < 1$. Also, it's easy to check $\mathcal{F}(u_2) > \mathcal{F}(u_3) > 1$, thus one has

$$J_W^{\text{FL}} = J_W \sqrt{\mathcal{F}(u_2)}, \quad \phi = \arccos u_2, \quad (34)$$

which explicitly gives the enlarged Walker limit by the FL-SOT. To be more intuitive, we plot J_W^{FL} and the corresponding $\phi (= \arccos u_2)$ in figure 2a and 2b, which perfectly reproduce existing numerics (for example figure 3a in Ref. [73]).

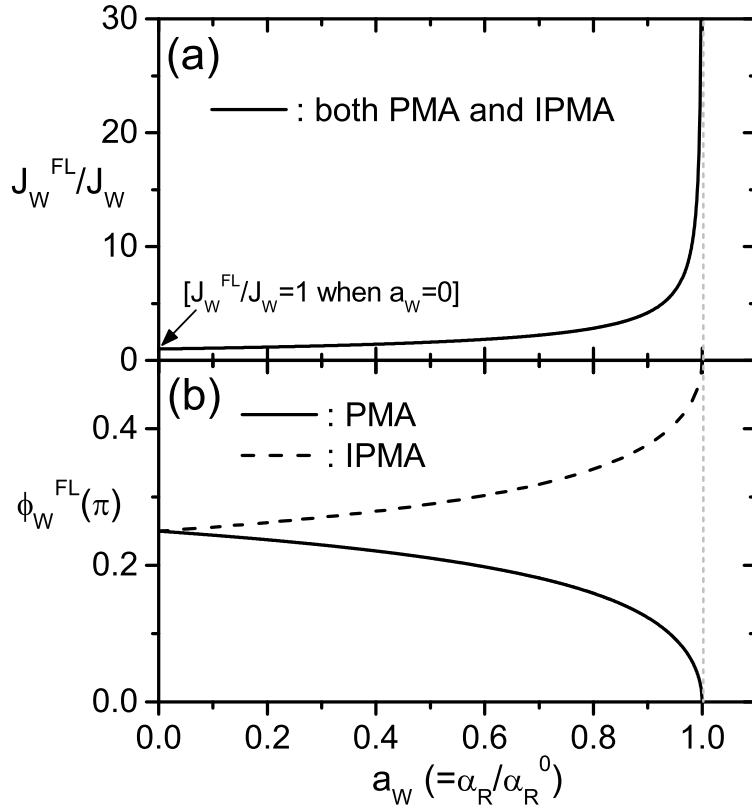


Figure 2. Walker breakdown suppression by FL-SOT as the function of parameter $a_W (= \alpha_R / \alpha_R^0$ when Rashba SOT solely contributes to FL-SOT) in the absence of i-DMI: (a) Enlarged Walker limits normalized by J_W which are the same for PMA and IPMA cases under the same a_W . (b) The azimuthal angle at which the enlarged Walker limit achieves. The solid and dashed curves are for PMA and IPMA systems, respectively. The gray short-dashed line indicates the occurrence of UAWB when $a_W \geq 1$. In all calculations we have set $\eta \text{sgn}(\alpha - \beta) = -1$.

Next we calculate the divergent behavior of J_W^{FL} when $a_W \rightarrow 1^-$. Define $\theta_0 \equiv \arccos(27 \cdot 1^2/16 - 1) = \arccos(11/16)$, which satisfies $\cos(\theta_0/3 + \pi/3) = 1/4$. Suppose $1 - a_W \equiv \epsilon \rightarrow 0^+$, it turns out $u_2 = 1 - \epsilon + o(\epsilon)$ from series expansions. Putting u_2 back into equation (34), after standard series-expansion calculation one gets

$$J_W^{\text{FL}} \approx \sqrt{2} J_W \cdot (1 - a_W)^{-1/2}, \quad (35)$$

with the corresponding ϕ satisfying

$$\phi \approx \sqrt{2} \cdot (1 - a_W)^{1/2}. \quad (36)$$

Equations (35) and (36) perfectly describe the asymptotic behaviors in figure 2a as $a_W \rightarrow 1^-$. This confirms the UAWB under appropriate combination of system parameters (H_K and H_{FL}). Also, when $a_W \rightarrow 1^-$ one has $u_3 \rightarrow (1 - \sqrt{5})/2 \approx -0.618$ and $\sqrt{\mathcal{F}(u_3)} \rightarrow 2^{-3/2}(\sqrt{5} - 1)^{5/2} \approx 0.6006$. This is a local maximum and will be abandoned as $|j_a| \rightarrow J_W^{\text{FL}}$.

Furthermore, in equation (30) for fixed α, β [thus fixed $\text{sgn}(\alpha - \beta)$] and j_a , the “ $\eta \rightarrow -\eta$ ” transformation is equivalent to “ $\phi \rightarrow \pi - \phi$ ”. This means the sign-inversion in topological charge does not change the polarity of a stable traveling wave.

To make the above mathematics more physical, here we take a limit case in which the Rashba effective field[46, 47]

$$\mathbf{H}_R = \lambda \left(\mathbf{e}_z \times \hat{\mathbf{J}} \right), \quad \lambda \equiv \frac{\alpha_R P}{\mu_B M_s} j_a, \quad (37)$$

solely contributes to H_{FL} . Here α_R is the Rashba parameter describing the Rashba SOC strength. The resulting λ is the conversion factor from current density to the Rashba field and is about $10^{-8} \sim 10^{-9}$ T cm²/A[25, 26]. Then the definition of a_W in equation (29) can be rewritten as

$$a_W = \frac{\alpha_R}{\alpha_R^0}, \quad \alpha_R^0 \equiv \frac{|\alpha - \beta|}{\alpha} \cdot \frac{1}{\Delta} \cdot \frac{2\mu_B^2}{\pi e \gamma}. \quad (38)$$

For magnetic parameters of Co-Ni FMM which is a typical PMA material (see the first column of Table 1, adopted from Ref. [79]), one has $\alpha_R^0 = 9.54$ meV · nm. Hence the above result means that for strong enough Rashba SOC ($|\alpha_R| \geq \alpha_R^0$), the UAWB occurs, while for $|\alpha_R| < \alpha_R^0$ the Walker limit is finitely enlarged as described in equation (34). For this reason, the horizontal axis of figure 2 can also be set as “ α_R/α_R^0 ”.

In addition, the critical condition “ $a_W = 1$ ” leads to “ $\alpha_R^{\text{th}} \propto |\beta/\alpha - 1|$ ” relationship in the threshold above which no Walker breakdown occurs, thus explicates existing numerical simulations, for example figure 3b in Ref. [73].

At last, for IPMA systems all the definitions and discussion are the same except for that the enlarged Walker limit achieves at $\phi = \arcsin u_2$. When $a_W \rightarrow 1^-$ the asymptotic behavior of ϕ turns to

$$\phi \approx \pi/2 - \sqrt{2} \cdot (1 - a_W)^{1/2}. \quad (39)$$

On the other hand, for magnetic parameters of permalloy FMM which is a typical IPMA material (see the second column of Table 1, adopted from Ref. [74]), one has a smaller critical Rashba parameter $\alpha_R^0 = 0.64$ meV · nm due to the relatively large wall width. This means that in IPMA systems, the UAWB is more likely to occur.

Table 1. Magnetic parameters used for numerical calculation and estimations. The first (second) column comes from Co-Ni (Py) which constitutes a typical PMA (IPMA) FMM layer in trilayers.

Magnetic parameter	Co-Ni (from Ref. [79])	Py (from Ref. [74])	unit
gyromagnetic ratio (γ):	1.76	1.76	10^{11} Hz/T
saturation magnetization (M_s):	1.0	0.8	10^6 A/m
FMM length :		2000	nm
FMM width :		80	nm
FMM thickness (t_F):	1.2	4	nm
hard axis anisotropy (k_H):	$1/\pi$	$0.8555 (=D_y - D_x)$	
domain wall width (Δ):	4	30	nm
i-DMI magnitude (D):	-1.4		mJ/m ²
Gilbert damping (α):	0.25	0.02	
spin polarization (P):	0.5	0.7	
nonadiabacity parameter (β):	0.5	0.01	
Rashba parameter (α_R):	6.3		meV · nm
spin Hall angle (θ_{SH}):	0.1	0.1	

3.4. Coexistence of STT and i-DMI

In this subsection, we study whether i-DMI itself can lead to UAWB, thus we have $a = 0$ and $b \neq 0$. As usual, we first focus on PMA systems. By setting $\cos \phi \equiv s \in [-1, +1]$, another function $\mathcal{G}(s)$ can be defined from (28) as

$$\mathcal{G}(s) \equiv (j_a/J_W)^2 = (1 - s^2)(2s - b)^2. \quad (40)$$

$\mathcal{G}(s)$ is also nonnegative and only equals to zero when $s = \pm 1$ or $b/2$. By requiring $\mathcal{G}'(s) = 0$, three extremal sites are obtained

$$s_1 = \frac{b}{2}, \quad s_2 = \frac{b + \sqrt{b^2 + 32}}{8}, \quad s_3 = -\frac{4}{b + \sqrt{b^2 + 32}}. \quad (41)$$

Standard calculus tells us that function $\mathcal{G}(s)$ always approaches maximum at $s = s_3$ when $b > 0$ ($s = s_2$ for $b < 0$). Then the modified Walker limit [maximum absolute value of the right hand side of equation (40)] and the corresponding ϕ reads

$$J_W^{\text{DM}} = J_W \sqrt{\mathcal{G}(s_3)}, \quad \phi = \arccos s_3. \quad (42)$$

Meanwhile, simple calculation yields that $7b^2/8 + 1 < \mathcal{G}(s_3) < b^2 + 5$, which confirms the Walker breakdown suppression effect at finite b (i.e. i-DMI). However since no singularities appear, UAWB does not occur under the pure action of finite i-DMI.

For IPMA systems, again the definitions and discussions are similar. The enlarged Walker limit can be described by equation (42) except for that the corresponding extremum point locates at $\phi = \arcsin s_3$.

Also, one should note that although the enlarged Walker limits in PMA and IPMA cases share the same analytical form, they will take different value under the same i-DMI strength D . To see this, we rewrite the definition of b in equation (27) as

$$b = \frac{\eta D}{D_0}, \quad D_0 \equiv \frac{\mu_0 M_s H_K \Delta}{\pi}. \quad (43)$$

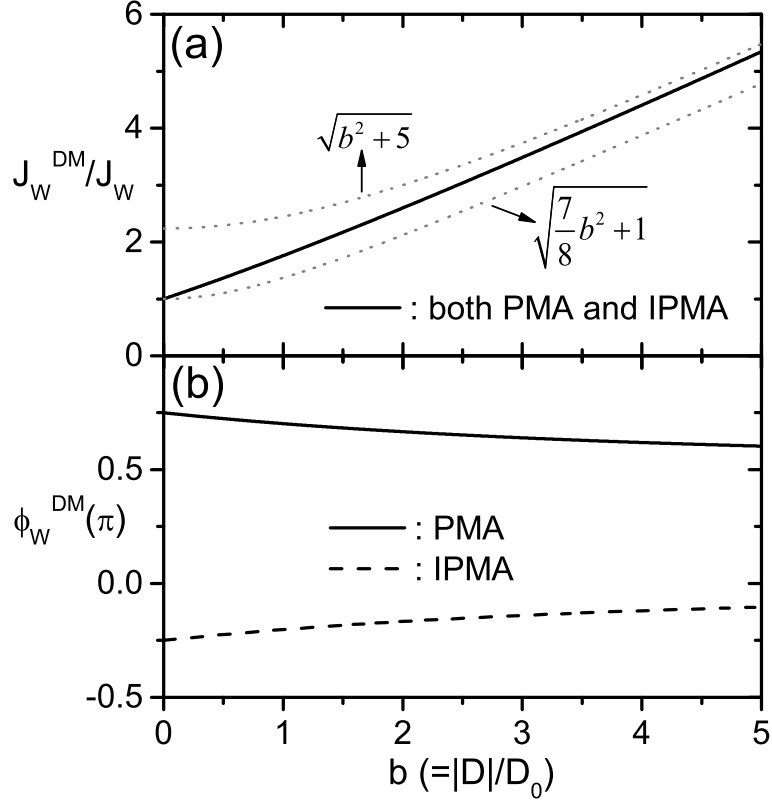


Figure 3. Walker breakdown suppression by pure i-DMI as the function of parameter $b (= |D|/D_0)$ in the absence of any SOTs: (a) Enlarged Walker limits normalized by J_W which are the same for PMA and IPMA systems under the same b . The gray dotted curves indicate the upper and lower boundaries. (b) The azimuthal angle at which the enlarged Walker limit achieves. The solid and dashed curves are for PMA and IPMA systems, respectively. In all calculations, $\eta \text{sgn}(\alpha - \beta) = -1$ and $\eta \text{sgn}(D) = +1$.

For Co-Ni FMM (PMA), one has $D_0 = 0.51 \text{mJ/m}^2$. While for Py FMM (IPMA), one gets $D_0 = 6.57 \text{mJ/m}^2$ due to the larger wall width therein. Thus generally i-DMI induces stronger Walker breakdown suppression in PMA systems under the same i-DMI strength D . In figure 3a and 3b, we plot J_W^{DM} and the corresponding ϕ for $0 \leq b \leq 5$ when $\eta \text{sgn}(D) = +1$. Clearly, the behaviors of enlarged Walker limits in figure 2a and figure 3a are totally different.

The qualitative role of FL-SOTs and i-DMI has been extensively discussed and now is clear. The driving current pulls the magnetization out of the easy plane, while the demagnetization field (H_K) tends to prevent this from happening, leading to the classical Walker limit H_W . The extra effective field from SOC (H_{FL}) and i-DMI in \mathbf{e}_y axis (hold for both PMA and IPMA cases) also helps to prevent the magnetization from leaving the easy plane, thus extending the traveling-wave region of walls. This is the physical origin of Walker breakdown suppression. Our analytics here provides detailed and solid foundation for the above physical picture.

4. Mobility change by ADL-SOT

To understand the mobility change and even its sign-inversion of Néel walls in FMM layer of trilayers in quite a lot experiments and simulations, the ADL-SOT must be appended. With the coexistence of STT, FL-SOT, ADL-SOT and i-DMI, the traveling-wave ansatz in equation (18) is again selected as the start-point of investigation. We will show that unlike the similarity in “Walker breakdown suppression” part, the mobility changes by ADL-SOT take quite different forms for PMA and IPMA cases.

4.1. General framework under the coexistence of STT, FL-SOT, ADL-SOT and i-DMI

As usual, we first concentrate on PMA cases. Under the traveling-wave ansatz, one has

$$\begin{aligned}\tilde{A} &= \frac{2\eta D}{\mu_0 M_s \Delta} \sin^2 \theta \sin \phi - \frac{H_K}{2} \sin \theta \sin 2\phi + H_{\text{FL}} \cos \phi \\ &\quad + H_{\text{ADL}} \cos \theta \sin \phi, \\ \tilde{B} &= H_{\text{ADL}} \cos \phi - H_{\text{FL}} \cos \theta \sin \phi.\end{aligned}\tag{44}$$

After putting back into the scalar LLG equations and integrating over the whole strip, it turns out

$$\begin{aligned}\frac{v(t)}{\Delta(\phi)} &= \frac{\eta\gamma(\mathcal{H} + \alpha\pi H_{\text{ADL}} \cos \phi)}{2(1 + \alpha^2)} - \frac{1 + \alpha\beta}{1 + \alpha^2} \frac{B_J}{\Delta(\phi)}, \\ \dot{\phi} &= -\frac{\alpha\gamma(\mathcal{H} - \pi H_{\text{ADL}} \cos \phi/\alpha)}{2(1 + \alpha^2)} + \frac{\alpha - \beta}{1 + \alpha^2} \frac{\eta B_J}{\Delta(\phi)},\end{aligned}\tag{45}$$

with the same functional $\mathcal{H}(H_K, H_{\text{FL}}, D, \phi)$ defined in equation (26). Note that the structure of equation (45) is different from that of equation (20) due to the presence of H_{ADL} -terms.

By requiring $\dot{\phi} = 0$ in equation (45), one gets

$$\sin 2\phi - b \sin \phi - c \cos \phi = \eta \text{sgn}(\alpha - \beta) \frac{j_a}{J_W}, \quad c \equiv \pi \frac{H_{\text{FL}}}{H_K} \left(1 + \frac{H_{\text{ADL}}}{\alpha H_{\text{FL}}}\right),\tag{46}$$

Since H_{FL} and H_{ADL} are both proportional to j_a , we set $(H_{\text{FL}})_W$ and $(H_{\text{ADL}})_W$ as the absolute effective-field strengths of FL- and ADL-SOTs when $|j_a| = J_W$, respectively. Then after defining

$$c_W \equiv \pi [(H_{\text{FL}})_W + \alpha^{-1} (H_{\text{ADL}})_W] / H_K > 0,\tag{47}$$

equation (46) is rewritten as

$$\frac{j_a}{J_W} = \frac{\sin 2\phi - b \sin \phi}{\eta \text{sgn}(\alpha - \beta) + c_W \cos \phi}.\tag{48}$$

The rest discussion on Walker breakdown suppression is the same as those in section 3.2 to section 3.4. We define the enlarged Walker limit as J_W^{all} . For $|j_a| \leq J_W^{\text{all}}$, from equation (45), the wall velocity reads

$$v = -\frac{\beta}{\alpha} B_J + \frac{\eta\gamma\pi\Delta}{2\alpha} H_{\text{ADL}} \cos \phi.\tag{49}$$

As for IPMA systems, after similar discussion, the existence condition of traveling-wave mode , $\dot{\phi} = 0$, provides

$$\sin 2\phi - b \cos \phi + c \sin \phi = \eta \text{sgn}(\alpha - \beta) \frac{j_a}{J_W}, \quad (50)$$

and the corresponding wall velocity reads

$$v = -\frac{\beta}{\alpha} B_J - \frac{\eta \gamma \pi \Delta}{2\alpha} H_{\text{ADL}} \sin \phi. \quad (51)$$

4.2. Mobility change in PMA systems

In principle, to obtain the wall velocity in traveling-wave mode, one should solve ϕ from its existence condition [for PMA systems, equation (46)] and then put it into the velocity formula [see equation (49)]. However the calculation process is hopelessly complicated.

Inspired by the asymptotic approach[81, 82, 83, 84, 85], we consider the case where $|j_a| \ll J_W^{\text{all}}$ thus the wall must be in traveling-wave mode ($\dot{\phi} = 0$) and ϕ is not far from its static position ($\phi_0 = \arccos[-\eta \text{sgn}(D)]$). Next we introduce the azimuthal deviation (see figure 1a)

$$\psi \equiv \phi - \phi_0. \quad (52)$$

Since $|\psi| \ll 1$, thus $\sin \phi \approx [-\eta \text{sgn}(D)]\psi$, $\cos \phi \approx -\eta \text{sgn}(D)$ and $\sin 2\phi \approx 2\psi$. Putting them into equation (46), the azimuthal deviation ψ can be solved as

$$\psi \approx \eta \frac{\text{sgn}(\alpha - \beta) - \text{sgn}(D)c_W}{2 + |D|/D_0} \frac{j_a}{j_W}. \quad (53)$$

Meanwhile the wall velocity in equation (49) becomes

$$v = -\frac{\beta}{\alpha} \frac{\mu_B P}{e M_s} j_a + \frac{-\text{sgn}(D)\gamma\pi\Delta}{2\alpha} H_{\text{ADL}}. \quad (54)$$

Since H_{ADL} is proportional to j_a , thus the wall mobility can be changed.

One extreme case is that ADL-SOT is induced solely by SHE. Thus $H_{\text{ADL}} = H_{\text{SHE}} = \hbar\theta_{\text{SH}}/(2\mu_0 e M_s t_F)$. Then equation (54) turns to

$$\frac{v_{\text{PMA}}}{v_{\text{STT}}} = 1 + \frac{\text{sgn}(D)\theta_{\text{SH}}}{\theta_{\text{SH}}^0}, \quad v_{\text{STT}} \equiv -\frac{\beta}{\alpha} B_J, \quad (55)$$

in which $\theta_{\text{SH}}^0 \equiv 2\beta P \mu_0 e t_F / (\gamma \pi m_e \Delta)$ and m_e is the electron mass. As long as $[-\text{sgn}(D)]\theta_{\text{SH}} > \theta_{\text{SH}}^0$, the motion direction of the wall will be reversed ($v_{\text{PMA}}/v_{\text{STT}} < 0$). Note that to achieve this, not only the strength but also the sign of spin Hall angle should be specified. This former is controlled by the ADL-SOT strength while the latter is selected by the sign of i-DMI parameter. For Co-Ni FMM, one has $\text{sgn}(D) = -1$ and $\theta_{\text{SH}}^0 \approx 0.048 < 0.1 = [-\text{sgn}(D)]\theta_{\text{SH}}$. Therefore Néel walls in this trilayer will move along charge current direction. In addition, by carefully arranging magnetic parameters [β , Δ , t_F and $\text{sgn}(D)$] of trilayer systems, $|v_{\text{PMA}}/v_{\text{STT}}|$ can be much higher than 1. This will help to explain the relatively high velocity of domain walls in Pt(3 nm)/Co(0.6 nm)/AlO_x(2 nm) trilayer (~ 400 m/s when $j_a \sim 10^8$ A/cm²)[37].

4.3. Mobility change in IPMA systems

As indicated in section 2.2, in IPMA cases the i-DMI does not select wall polarity thus $\phi_0 = k\pi, k \in \mathbb{Z}$, i.e. $\cos \phi_0 = (-1)^k$. Again we introduce the azimuthal deviation $\psi \equiv \phi - \phi_0$ under small current density. Since $|\psi| \ll 1$, thus $\sin \phi \approx (-1)^k \psi$, $\cos \phi \approx (-1)^k$ and $\sin 2\phi \approx 2\psi$. Putting them into equation (50), one has

$$\psi \approx \eta \left[\frac{(\alpha - \beta)B_J}{\gamma\Delta H_W} + \frac{(-1)^k D}{D_0} \right] \cdot \left[2 + \frac{(-1)^k \pi}{H_K} \left(H_{\text{FL}} + \frac{H_{\text{ADL}}}{\alpha} \right) \right]^{-1}. \quad (56)$$

Meanwhile the wall velocity is reduced to

$$v = -\frac{\beta}{\alpha} B_J - \frac{\eta\gamma\pi\Delta}{2\alpha} H_{\text{ADL}} (-1)^k \psi, \quad (57)$$

which is complicated due to the coexistence of H_{FL} , H_{ADL} and D .

Next we consider an extreme case where the i-DMI is neglected. After simple algebra, the wall velocity in equation (57) becomes

$$\frac{v_{\text{IPMA}}}{v_{\text{STT}}} = \frac{1 + \frac{(-1)^k \pi H_{\text{ADL}}}{2H_K} (\zeta + \beta^{-1})}{1 + \frac{(-1)^k \pi H_{\text{ADL}}}{2H_K} (\zeta + \alpha^{-1})}, \quad (58)$$

with $\zeta \equiv H_{\text{FL}}/H_{\text{ADL}}$ and can be assumed positive without losing generality. *Obviously, the presence of H_{ADL} as well as the condition $\alpha \neq \beta$ provides us the possibility of changing wall mobility.* Interestingly, the direction of wall motion can even be reversed ($v_{\text{IPMA}}/v_{\text{STT}} < 0$) under the following condition

$$\frac{1}{\zeta + \max(\frac{1}{\alpha}, \frac{1}{\beta})} < \frac{(-1)^{k+1} \pi H_{\text{ADL}}}{2H_K} < \frac{1}{\zeta + \min(\frac{1}{\alpha}, \frac{1}{\beta})}. \quad (59)$$

In addition, the wall halts at $(-1)^{k+1} \pi H_{\text{ADL}} = 2H_K/(\zeta + \beta^{-1})$ and a velocity divergence occurs at $(-1)^{k+1} \pi H_{\text{ADL}} = 2H_K/(\zeta + \alpha^{-1})$.

Equation (59) shows that only walls with polarity satisfying $(-1)^{k+1} H_{\text{ADL}} > 0$ can be reversed from electron flow to charge current direction, which well explains the ‘‘polarity sensitivity’’ phenomena in IPMA systems. On the other hand, in real IPMA materials $\alpha, \beta \ll 1$. Therefore the current density under which equation (59) holds can be small enough to ensure the approximation for obtaining equation (56), thus makes the whole deduction coherent.

To numerically check our analytics, in the simplest case we set $H_{\text{FL}} = 0$ (thus $\zeta = 0$) and suppose that H_{ADL} solely comes from SHE, which is exactly the case in Ref. [74]. Under the magnetic parameters in the second column of Table 1, the ‘‘ $v_{\text{IPMA}}(v_{\text{STT}}) \sim j_a$ ’’ curves are plotted in figure 4. The black line indicates the linear dependence of v_{STT} on j_a , while the red curve represent the wall velocity v_{IPMA} when only SHE-induced ADL-SOT is considered. The reversal region is $-\alpha J_0 < j_a < -\beta J_0$ with $\alpha = 0.02$, $\beta = 0.01$ and $J_0 \equiv 4\mu_0 e k_H M_s^2 t_F / (\pi \hbar \theta_{\text{SH}}) = 5.32 \times 10^{13}$ A/m². The wall-halt current is $-\beta J_0 = -5.32 \times 10^{11}$ A/m² and the velocity-divergence current is $-\alpha J_0 = -1.064 \times 10^{12}$ A/m². All these results reproduce very well the ‘‘ $\theta_{\text{SH}} = +0.1$ ’’ case in figure 3a of Ref. [74]. In addition, the positively divergent part for ‘‘ $j_a < -\alpha J_0$ ’’ in figure 4 indicates the

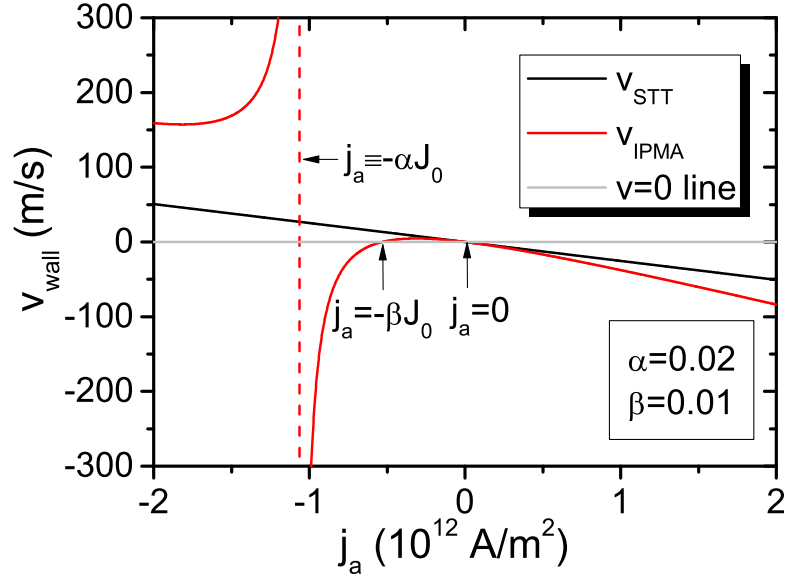


Figure 4. (Color online) Mobility change and motion-direction reversal in the presence of ADL-SOT for $\alpha > \beta$. Here $\alpha = 0.02$, $\beta = 0.01$ and $D = 0$. Other magnetic parameters are taken as those in the second column of Table 1. The solid black line and red curve indicate v_{STT} and v_{IPMA} , respectively. The vertical dash line is the $j_a \equiv -\alpha J_0$ line where divergence in v_{IPMA} occurs.

possibility of “velocity boosting” in the original direction (electron flow) by SHE-induced ADL-SOTs. There are few reports in literatures about this and should be worth of more efforts in both simulations and experiments. In particular, it may help to explain the unexpected high velocities of domain walls in permalloy layer of multilayer films in some early works[86].

4.4. Discussions

All analytics in this work are performed based on the traveling-wave ansatz in equation (18). One must bear in mind that it is rigorous only in the absence of any SOTs and i-DMI, otherwise in principle it fails to provide the rigorous wall profile. However, it may serve as a “not-bad” approximation of the actual magnetization texture in trilayers. This has been numerically tested in Ref. [79].

Second, as this ansatz can not hold everywhere along the long axis of strip, to obtain the collective behaviors we then integrate it over $r \in (-\infty, +\infty)$ which is transferred to the integration of $\theta \in (0, \pi)$. However, when j_a increases, effective transverse fields from SOTs and i-DMI will pull the magnetization in two faraway domains away from strip axis. Then the integration of $r \in (-\infty, +\infty)$ should be converted to that of θ over $(\theta_0, \pi - \theta_0)$, where θ_0 is positively correlated with j_a with some complicated mathematical dependence. For simplicity, we have not considered this θ_0 in the above sections. Further investigation on this issue is out of the scope of this work.

At last, by “small quantity analysis” we succeed in explaining the mobility change in both PMA and IPMA systems. In particular, the sign-inversion of mobility as well as the “polarity sensitivity” therein is recovered analytically. In real experiments, the motion-direction-reversal behavior is observed in a relatively wide range of j_a (thus H_{ADL}). This should not be regarded as a contradiction with equation (59) since it is obtained under the assumption $|j_a| \ll J_W^{\text{all}}$. In fact, the necessity of ADL-SOTs for mobility sign-inversion, as well as the polarity selection rule therein, should be the main focus in this subsection. Also, this is one of the main reasons why this part of SOT is named as “anti-damping-like” since they can input energy into the system, not just dissipate it.

5. Summary

In this work, we analytically investigate the current-induced domain wall dynamics in HM/FMM/Oxide trilayers with strong SOCs and i-DMI. We show that in both PMA and IPMA systems, FL-SOT can induce UAWB but i-DMI can not. For moderate FL-SOT and arbitrary i-DMI strength, we provide analytical expressions of the finitely enlarged Walker limits. On the other hand, the wall mobility change can be explained only when ADL-SOT is included under the coexistence of STT, SOT and i-DMI. In particular, for PMA systems strong enough spin Hall angle and appropriate sign of i-DMI parameter will lead to sign-inversion in wall mobility even under small enough current density, while for IPMA systems this will only occur when current density falls into a finite range. These analytical results provide insights not only for explaining existing experimental and numerical data (in fact a numbers of them have been explained in the main text), but also for the development of future domain-wall-based magnetic nanodevices.

Acknowledgments

This work is supported by the National Natural Science Foundation of China (Grants Nos. 51671148, 11674251, 51601132 and 11374088). J. Lu also acknowledges the support from the Natural Science Foundation of Hebei Province, China (Grant No. A2014205080), and the Science Foundation for The Excellent Youth Scholars of Educational Commission of Hebei Province, China (Grant No. Y2012027).

References

- [1] Berger L 1996 Emission of spin waves by a magnetic multilayer traversed by a current *Phys. Rev. B* **54** 9353
- [2] Slonczewski J 1996 Current-driven excitation of magnetic multilayers *J. Magn. Magn. Mater.* **159** L1-L7
- [3] Bazaliy Ya B, Jones B A and Zhang S -C 1998 Modification of the Landau-Lifshitz equation in the presence of a spin-polarized current in colossal- and giant-magnetoresistive materials *Phys. Rev. B* **57** R3213(R)

- [4] Stiles M D and Zangwill A 2002 Anatomy of spin-transfer torque *Phys. Rev. B* **66** 014407
- [5] Tatara G and Kohno H 2004 Theory of current-driven domain wall motion: spin transfer versus momentum transfer *Phys. Rev. Lett.* **92** 086601
- [6] Li Z and Zhang S 2004 Domain-wall dynamics and spin-wave excitations with spin-transfer torques *Phys. Rev. Lett.* **92** 207203
- [7] Zhang S and Li Z 2004 Roles of nonequilibrium conduction electrons on the magnetization dynamics of ferromagnets *Phys. Rev. Lett.* **93** 127204
- [8] Thiaville A, Nakatani Y, Miltat J and Suzuki Y 2005 Micromagnetic understanding of current-driven domain wall motion in patterned nanowires *Europhys. Lett.* **69** 990
- [9] Yan P, Sun Z Z, Schliemann J and Wang X R 2010 Optimal spin current pattern for fast domain wall propagation in nanowires *Europhys. Lett.* **92** 27004
- [10] Sun Z Z, Schliemann J, Yan P and Wang X R 2011 Current-induced domain wall motion with adiabatic and nonadiabatic spin torques in magnetic nanowires *Eur. Phys. J. B* **79** 449
- [11] Grollier J, Boulenc P, Cros V, Hamzić A, Vaurès A, Fert A and Faini G 2003 Switching a spin valve back and forth by current-induced domain wall motion *Appl. Phys. Lett.* **83** 509
- [12] Yamaguchi A, Ono T, Nasu S, Miyake K, Mibu K and Shinjo T 2004 Real-space observation of current-driven domain wall motion in submicron magnetic wires *Phys. Rev. Lett.* **92** 077205
- [13] Kläui M, Jubert P -O, Allenspach R, Bischof A, Bland J A C, Faini G, Rüdiger U, Vaz C A F, Vila L and C. Vouille C 2005 Direct observation of domain-wall configurations transformed by spin currents *Phys. Rev. Lett.* **95** 026601
- [14] Marrows C H 2005 Spin-polarised currents and magnetic domain walls *Adv. Phys.* **54** 585
- [15] Hayashi M, Thomas L, Rettner C, Moriya R, Bazaliy Y B and Parkin S S P 2007 Current driven domain wall velocities exceeding the spin angular momentum transfer rate in Permalloy nanowires *Phys. Rev. Lett.* **98** 037204
- [16] Parkin S S P, Hayashi M and Thomas L 2008 Magnetic domain-wall racetrack memory *Science* **320** 190
- [17] Parkin S S P and Yang S -H 2015 Memory on the racetrack *Nat. Nanotechnol.* **10** 195
- [18] Hayashi M, Thomas L, Moriya R, Rettner C and Parkin S S P 2008 Current-controlled magnetic domain-wall nanowire shift register *Science* **320** 209
- [19] Franken J H, Swagten H J M and Koopmans B 2012 Shift registers based on magnetic domain wall ratchets with perpendicular anisotropy *Nat. Nanotechnol.* **7** 499
- [20] Wang X, Chen Y, Xi H, Li H and Dimitrov D 2009 Spintronic memristor through spin-torque-induced magnetization motion *IEEE Elec. Dev. Lett.* **30** 294
- [21] Münchenberger J, Reiss G and Thomas A 2012 A memristor based on current-induced domain-wall motion in a nanostructured giant magnetoresistance device *J. Appl. Phys.* **111** 07D303
- [22] Khvalkovskiy A V, Zvezdin K A, Gorbunov Ya V, Cros V, Grollier J, Fert A and Zvezdin A K 2009 High domain wall velocities due to spin currents perpendicular to the plane *Phys. Rev. Lett.* **102** 067206
- [23] Boone C T, Katine J A, Carey M, Childress J R, Cheng X and Krivorotov I N 2010 Rapid domain wall motion in Permalloy nanowires excited by a spin-polarized current applied perpendicular to the nanowire *Phys. Rev. Lett.* **104** 097203
- [24] Chanthbouala A, Matsumoto R, Grollier J, Cros V, Anane A, Fert A, Khvalkovskiy A V, Zvezdin K A, Nishimura K, Nagamine Y, Maehara H, Tsunekawa K, Fukushima A and Yuasa S 2011 Vertical-current-induced domain-wall motion in MgO-based magnetic tunnel junctions with low current densities *Nat. Phys.* **7** 626
- [25] Miron I M, Gaudin G, Auffret S, Rodmacq B, Schuhl A, Pizzini S, Vogel J and Gambardella P 2010 Current-driven spin torque induced by the Rashba effect in a ferromagnetic metal layer *Nat. Mater.* **9** 230
- [26] Pi U H, Kim K W, Bae J Y, Lee S C, Cho Y J, Kim K S and Seo S 2010 Tilting of the spin orientation induced by Rashba effect in ferromagnetic metal layer *Appl. Phys. Lett.* **97** 162507
- [27] Liu L, Pai C -F, Li Y, Tseng H W, Ralph D C and Buhrman R A 2012 Spin-torque switching with

- the giant spin Hall effect of Tantalum *Science* **336** 555
- [28] Liu L, Lee O J, Gudmundsen T J, Ralph D C and Buhrman R A 2012 Current-induced switching of perpendicularly magnetized magnetic layers using spin torque from the spin Hall effect *Phys. Rev. Lett.* **109** 096602
- [29] Garello K, Miron I M, Avci C O, Freimuth F, Mokrousov Y, Blügel S, Auffret S, Boulle O, Gaudin G and Gambardella P 2013 Symmetry and magnitude of spinorbit torques in ferromagnetic heterostructures *Nat. Nanotechnol.* **8** 587
- [30] Nguyen M -H, Ralph D C and Buhrman R A 2016 Spin torque study of the spin Hall conductivity and spin diffusion length in Platinum thin films with varying resistivity *Phys. Rev. Lett.* **116** 126601
- [31] Ou Y, Pai C -F, Shi S, Ralph D C and Buhrman R A 2016 Origin of fieldlike spin-orbit torques in heavy metal/ferromagnet/oxide thin film heterostructures *Phys. Rev. B* **94** 140414
- [32] Ghosh A, Garello K, Avci C O, Gabureac M and Gambardella P 2017 Interface-Enhanced Spin-Orbit Torques and Current-Induced Magnetization Switching of Pd/Co/AlO_x Layers *Phys. Rev. Appl.* **7** 014004
- [33] Moore T A, Miron I M, Gaudin G, Serret G, Auffret S, Rodmacq B, Schuhl A, Pizzini S, Vogel J and Bonfim M 2008 High domain wall velocities induced by current in ultrathin Pt/Co/AlO_x wires with perpendicular magnetic anisotropy *Appl. Phys. Lett.* **93** 262504
- [34] Miron I M, Garello K, Gaudin G, Zermatten P -J, Costache M V, Auffret S, Bandiera S, Rodmacq B, Schuhl A and Gambardella P 2011 Perpendicular switching of a single ferromagnetic layer induced by in-plane current injection *Nature* **476** 189
- [35] Emori S, Bauer U, Ahn S -M, Martinez E and Beach G S D 2013 Current-driven dynamics of chiral ferromagnetic domain walls *Nat. Mater.* **12** 611
- [36] Lee J -C, Kim K -J, Ryu J, Moon K -W, Yun S -J, Gim G -H, Lee K -S, Shin K -H, Lee H -W and Choe S -B 2011 Universality classes of magnetic domain wall motion *Phys. Rev. Lett.* **107** 067201
- [37] Miron I M, Moore T, Szabolcs H, Buda-Prejbeanu L D, Auffret S, Rodmacq B, Pizzini S, Vogel J, Bonfim M, Schuhl A and Gaudin G 2011 Fast current-induced domain-wall motion controlled by the Rashba effect *Nat. Mater.* **10** 419
- [38] Emori S, Bono D C and Beach G S D 2012 Interfacial current-induced torques in Pt/Co/GdOx *Appl. Phys. Lett.* **101** 042405
- [39] Ryu K -S, Thomas L, Yang S -H and Parkin S S P 2012 Current induced tilting of domain walls in high velocity motion along perpendicularly magnetized micron-sized Co/Ni/Co racetracks *Appl. Phys. Express* **5** 093006
- [40] Lavrijsen R, Haazen P P J, Murè E, Franken J H, Kohlhepp J T, Swagten H J M and Koopmans B 2012 Asymmetric Pt/Co/Pt-stack induced sign-control of current-induced magnetic domain-wall creep *Appl. Phys. Lett.* **100** 262408
- [41] Ryu K -S, Thomas L, Yang S -H and Parkin S S P 2013 Chiral spin torque at magnetic domain walls *Nat. Nanotechnol.* **8** 527
- [42] Linder J and Alidoust M 2013 Asymmetric ferromagnetic resonance, universal Walker breakdown, and counterflow domain wall motion in the presence of multiple spin-orbit torques *Phys. Rev. B* **88** 064420
- [43] Martinez E, Finocchio G, Torres L and Lopez-Diaz L 2013 The influence of the spin-orbit torques on the current-driven domain wall motion *AIP Advances* **3** 072109
- [44] Boulle O, Buda-Prejbeanu L D, Jué E, Miron I M and Gaudin G 2014 Current induced domain wall dynamics in the presence of spin orbit torques *J. Appl. Phys.* **115** 17D502
- [45] Stier M, Creutzburg M and Thorwart M 2014 Rashba-induced chirality switching of domain walls and suppression of the Walker breakdown *Phys. Rev. B* **90** 014433
- [46] Manchon A and Zhang S 2008 Theory of nonequilibrium intrinsic spin torque in a single nanomagnet *Phys. Rev. B* **78** 212405
- [47] Manchon A and Zhang S 2009 Theory of spin torque due to spin-orbit coupling *Phys. Rev. B* **79**

094422

- [48] Matos-Abiague A and Rodríguez-Suárez R L 2009 Spin-orbit coupling mediated spin torque in a single ferromagnetic layer *Phys. Rev. B* **80** 094424
- [49] Gambardella P and Miron I M 2011 Current-induced spinorbit torques *Philosophical Transactions of the Royal Society A* **369** 3175
- [50] Haney P M, Lee H -W, Lee K -J, Manchon A and Stiles M D 2013 Current-induced torques and interfacial spin-orbit coupling *Phys. Rev. B* **88** 214417
- [51] Haney P M, Lee H -W, Lee K -J, Manchon A and Stiles M D 2013 Current induced torques and interfacial spin-orbit coupling: Semiclassical modeling *Phys. Rev. B* **87** 174411
- [52] Wang X and Manchon A 2012 Diffusive spin dynamics in ferromagnetic thin films with a Rashba interaction *Phys. Rev. Lett.* **108** 117201
- [53] Kim K -W, Seo S -M, Ryu J, Lee K -J and Lee H -W 2012 Magnetization dynamics induced by in-plane currents in ultrathin magnetic nanostructures with Rashba spin-orbit coupling *Phys. Rev. B* **85** 180404
- [54] Pesin D A and MacDonald A H 2012 Quantum kinetic theory of current-induced torques in Rashba ferromagnets *Phys. Rev. B* **86** 014416
- [55] van der Bijl E and Duine R A 2012 Current-induced torques in textured Rashba ferromagnets *Phys. Rev. B* **86** 094406
- [56] Qaiumzadeh A, Duine R A and Titov M 2015 Spin-orbit torques in two-dimensional Rashba ferromagnets *Phys. Rev. B* **92** 014402
- [57] Kurebayashi H, Sinova J, Fang D, Irvine A C, Skinner T D, Wunderlich J, Novk V, Campion R P, Gallagher B L, Vehstedt E K, Zarbo L P, Vyborny K, Ferguson A J and Jungwirth T 2014 An antidamping spinorbit torque originating from the Berry curvature *Nat. Nanotechnol.* **9** 211
- [58] Li H, Gao H, Zárbo L P, Výborný K, Wang X, Garate I, Doğan F, Čejchan A, Sinova J, Jungwirth T and Manchon A 2015 Intraband and interband spin-orbit torques in noncentrosymmetric ferromagnets *Phys. Rev. B* **91** 134402
- [59] Chen W, Sigrist M, Sinova J and Manske D 2015 Minimal model of spin-transfer torque and spin pumping caused by the spin Hall effect *Phys. Rev. Lett.* **115** 217203
- [60] Hirsch J E 1999 Spin Hall effect *Phys. Rev. Lett.* **83** 1834
- [61] Freimuth F, Blügel S and Mokrousov Y 2014 Spin-orbit torques in Co/Pt(111) and Mn/W(001) magnetic bilayers from first principles *Phys. Rev. B* **90** 174423
- [62] Amin V P and Stiles M D 2016 Spin transport at interfaces with spin-orbit coupling: Formalism *Phys. Rev. B* **94** 104419
- [63] Amin V P and Stiles M D 2016 Spin transport at interfaces with spin-orbit coupling: Phenomenology *Phys. Rev. B* **94** 104420
- [64] Ado I A, Tretiakov O A and Titov M 2017 Microscopic theory of spin-orbit torques in two dimensions *Phys. Rev. B* **95** 094401
- [65] Dzyaloshinskii I E 1957 Thermodynamic theory of “weak” ferromagnetism in antiferromagnetic substances *JETP Lett.* **5** 1259
- [66] Moriya T 1960 Anisotropic superexchange interaction and weak ferromagnetism *Phys. Rev.* **120** 91
- [67] Dzyaloshinskii I E 1965 Theory of helicoidal structures in antiferromagnets *JETP Lett.* **20** 665
- [68] Linder J 2013 Chirality-sensitive domain wall motion in spin-orbit coupled ferromagnets *Phys. Rev. B* **87** 054434
- [69] Obata K and Tataru G 2008 Current-induced domain wall motion in Rashba spin-orbit system *Phys. Rev. B* **77** 214429
- [70] He P -B, Zhou Z -D, Wang R -X, Li Z -D, Cai M -Q and Pan A -L 2013 Stability analysis of current-driven domain wall in the presence of spin Hall effect *J. Appl. Phys.* **114** 093912
- [71] Martinez E 2012 Micromagnetic analysis of the Rashba field on current-induced domain wall propagation *J. Appl. Phys.* **111** 033901
- [72] Martinez E 2012 Static Properties and Current-Driven Dynamics of Domain Walls in Perpendicular

- Magnetocrystalline Anisotropy Nanostrips with Rectangular Cross-Section *Adv. Cond. Matter Phys.* **2012** 954196
- [73] Ryu J, Seo S -M, Lee K -J and Lee H -W 2012 Rashba spinorbit coupling effects on a current-induced domain wall motion *J. Magn. Magn. Mater.* **324** 1449
- [74] Seo S -M, Kim K -W, Ryu J, Lee H -W and Lee K -J 2012 Current-induced motion of a transverse magnetic domain wall in the presence of spin Hall effect *Appl. Phys. Lett.* **101** 022405
- [75] Khvalkovskiy A V, Cros V, Apalkov D, Nikitin V, Krounbi M, Zvezdin K A, Anane A, Grollier J and Fert A 2013 Matching domain-wall configuration and spin-orbit torques for efficient domain-wall motion *Phys. Rev. B* **87** 020402
- [76] Martinez E, Emori S and Beach G S D 2013 Current-driven domain wall motion along high perpendicular anisotropy multilayers: The role of the Rashba field, the spin Hall effect, and the Dzyaloshinskii-Moriya interaction *Appl. Phys. Lett.* **103** 072406
- [77] Martinez E, Emori S, Perez N, Torres L and Beach G S D 2014 Current-driven dynamics of Dzyaloshinskii domain walls in the presence of in-plane fields: Full micromagnetic and one-dimensional analysis *J. Appl. Phys.* **115** 213909
- [78] Gilbert T L 2004 A phenomenological theory of damping in ferromagnetic materials *IEEE Trans. Magn.* **40** 3443
- [79] Risinggård V and Linder J 2017 Universal absence of Walker breakdown and linear current-velocity relation via spin-orbit torques in coupled and single domain wall motion *Phys. Rev. B* **95** 134423
- [80] Schryer N L and Walker L R 1974 The motion of 180° domain walls in uniform dc magnetic fields *J. Appl. Phys.* **45** 5406
- [81] Goussev A, Lund R G, Robbins J M, Slastikov V and Sonnenberg C 2013 Fast domain-wall propagation in uniaxial nanowires with transverse fields *Phys. Rev. B* **88** 024425
- [82] Goussev A, Lund R G, Robbins J M, Slastikov V and Sonnenberg C 2013 Domain wall motion in magnetic nanowires: an asymptotic approach *Proc. R. Soc. A* **469** 20130308
- [83] Lu J 2016 Statics and field-driven dynamics of transverse domain walls in biaxial nanowires under uniform transverse magnetic fields *Phys. Rev. B* **93** 224406
- [84] Li M, Wang J B and Lu J 2017 General planar transverse domain walls realized by optimized transverse magnetic field pulses in magnetic biaxial nanowires *Sci. Rep.* **7** 43065
- [85] Yu M, Li M and Lu J 2019 Engineering planar transverse domain walls in biaxial magnetic nanostrips by tailoring transverse magnetic fields with uniform orientation *Nanomaterials* **9** 128
- [86] Hayashi M, Thomas L, Rettner C, Moriya R, Bazaliy Y B and Parkin S S P 2007 Current driven domain wall velocities exceeding the spin angular momentum transfer rate in permalloy nanowires *Phys. Rev. Lett.* **98** 037204